buildings

MDPI

Article

Energy Performances Assessment of Extruded and 3D Printed Polymers Integrated into Building Envelopes for a South Italian Case Study

Giovanni Ciampi *, Yorgos Spanodimitriou *, Michelangelo Scorpio, Antonio Rosato and Sergio Sibilio *

Department of Architecture and Industrial Design, University of Campania Luigi Vanvitelli, 81031 Aversa, Italy; michelangelo.scorpio@unicampania.it (M.S.); antonio.rosato@unicampania.it (A.R.)

* Correspondence: giovanni.ciampi@unicampania.it (G.C.); yorgos.spanodimitriou@unicampania.it (Y.S.); sergio.sibilio@unicampania.it (S.S.)

Abstract: Plastic materials are increasingly becoming used in the building envelope, despite a lack of investigation on their effects. In this work, an extruded Acrylonitrile-Butadiene-Styrene panel has been tested as a second-skin layer in a ventilated facade system using a full-scale facility. The experimental results show that it is possible to achieve performances very similar to conventional materials. A numerical model has then been developed and used to investigate the performances of plastic and composite polymer panels as second-skin layers. The experimental data has been used to verify the behavior of the numerical model, from a thermal point of view, showing good reliability, with a root mean square error lower than 0.40 °C. This model has then been applied in different refurbishment cases upon varying: the polymer and the manufacturing technology (extruded or 3D-printed panels). Eight refurbishment case studies have been carried out on a typical office building located in Napoli (Italy), by means of a dynamic simulation software. The simulation results show that the proposed actions allow the reduction of the thermal and cooling energy demand (up to 6.9% and 3.1%, respectively), as well as the non-renewable primary energy consumption (up to 2.6%), in comparison to the reference case study.

Keywords: ventilated facade; second-skin materials; 3D printed materials; additive manufacturing; TRNSYS; full-scale facility; retrofit action; energy saving

Citation: Ciampi, G.; Spanodimitriou, Y.; Scorpio, M.; Rosato, A.; Sibilio, S. Energy Performances Assessment of Extruded and 3D Printed Polymers Integrated into Building Envelopes for a South Italian Case Study. *Buildings* **2021**, *11*, 141. https://doi.org/10.3390/buildings11040141

Academic Editors: Alessandro Cannavale, Francesco Martellotta and Francesco Fiorito

Received: 18 February 2021
Accepted: 25 March 2021
Published: 1 April 2021

1. Introduction

Approximately 40% of the EU energy consumption can be directly attributed to the building sector, which is also responsible for about 36% of the greenhouse gas emissions [1,2]. In addition, in the EU-28, only 3% of the edifices have an efficient building envelope [3], mainly due to the fact that about 35% of the EU's buildings are over 50 years old and only around 1% of them are renovated each year [1]. Certainly, the constraints associated with the new buildings are fewer with respect to those associated with the refurbishment of existing constructions, so the new one allows for better-optimized design in terms of energy efficiency of the envelope [4]. However, in Italy, many buildings (about 4 million) were built in the early 1900s and about half of these have been classified as historical architectures and nowadays have been reused [5]. Therefore, in the Italian scenario, the improvement of the energetic performances of the existing building envelope represents a crucial aspect in the increasing of the building's energy efficiency and the indoor environmental quality on a large-scale [6]. In this context, different products and systems have been proposed to improve the buildings energy efficiency, visual and thermal comfort, as well as their sustainability [7–12] and, in recent years, the interest of the scientific community has seen an increase in the facade domain to improve the overall building energy efficiency [13]. In particular, the use of passive systems is raising more

and more interest in the building sector [7,8,14]. A passive building is one in which the indoor environment is not regulated by using mechanical heating and cooling systems, but by means of a conscious structure and architectural design of the envelope and its components [7]. In recent years, as part of a shift towards more energy-efficient buildings, a lot of different new facade technologies and solutions have been proposed for the improvement of their energy performance by the introduction of better insulation, shading devices, as well as a second-skin layer (double-skin facades [15,16], building integrated photovoltaic [17,18] and opaque ventilated facades [19,20]). Among these, the double-skin facade (DSF) and opaque ventilated facades (OVF) have been suggested as one of the best solutions, thanks to their ability to ensure better thermal performance and indoor environmental quality, as well as to improve the aesthetic appeal of buildings [15,16,19,20]. The concept of DSF was introduced in the early 1900s, but little progress was made until the 1990s [7,21]; it consists of a standard facade, an air cavity, and an additional external skin. The material used as a second-skin is usually glass [7,21]; however, a shading device can also be installed within the cavity between the two layers of the facade to control the solar radiation [7,21]. The OVFs are passive systems that consist of multiple layer construction (external second-skin, an intermediate air cavity, and an internal wall). The OVFs have been, more and more frequently, chosen by contractors, designers as well as architects for different typologies (offices, schools, residential) of new and renovated buildings as well as in different climates [19,20]. Several papers [22–29] investigated the energy performances of OVFs through simulation software (EnergyPlus [30] and TRNSYS [31], the most widely used), highlighting the benefits achievable by these systems. In addition, the literature review [22–29] highlights that the materials usually used as second-skin layer are: glass, porcelain stoneware tile, natural stone, aluminum, OSB, and composite panels.

Nowadays, there are always more innovative materials [32–35] used in architecture, also as a second-skin layer, even if evaluating their impact on the envelope's energy performance is a complex task [6,11]. In this work, plastic and composite polymers have been investigated with the aim to evaluate their integration in the building facade and their potential benefits achievable in refurbishment case studies.

1.1. Plastic and Composite Polymers in Building Facades

In recent years, the use of polymers in building and engineering has increased substantially, thanks to their: (i) ease of production, (ii) ease of installation, (iii) durability, (iv) low maintenance requirements, (v) lightweight nature and (vi) ability to be formed into complex shapes [34,35]. Moreover, polymers form good thermal and electrical insulators that are not affected by chemical and biological risks [35]. They have not only been used to replace the traditional construction materials (cement, brick, concrete, wood, metal, and glass), but these materials have also been used in a complementary way to improve the building envelope performance to satisfy the modern demands of both new projects and refurbishment ones [32–35]. From an aesthetic point of view, these materials are available in several colors and texture alternatives. Several applications of plastic and composite polymer walls in buildings were reported in the literature [33]. In [33], 23 examples of architecture were reported, demonstrating that plastic and composite polymers can be used in dwelling domes, large-span volumes or envelop large facade surfaces, and transparent sky-lights on the roofs of industrial buildings. Another example can be found in [36,37], where the designers have realized a temporary pavilion with an envelope made of double-walled transparent corrugated sheets of PolyEthylene Terephthalate (PET) recycled plastic. Similarly, in [38], a massive pavilion, designed as an exhibition hall for the 2010 Taipei International Flora Expo, has been built using recycled PET for the building envelope, also proving strong resistance to fires and earthquakes. As reported in [39], polycarbonate multi-sheet systems are increasing their share of the glazing market since they provide good performance while weighing and costing significantly less than glass. For these reasons, several studies have been conducted to assess their characteristics upon varying geometries and installation typology. In [39], the authors assessed the thermal and optical characteristics of different

polycarbonate sheets, highlighting a strong angular dependence in polycarbonate panels' optical properties, significantly different to the conventional multiple-layered glass, and a good overall thermal behavior. For these reasons, the polycarbonate could be used as a valid alternative, fulfilling the energy requirements and improving the visual comfort, reducing the glaring problem by diffusing the light, while providing more flexibility in the design and appearance of the buildings. In [40], a detailed experimental analysis of the thermal behavior of different polycarbonate multi-sheet systems has been carried out by varying the installation angle. The results highlighted a very low incidence of the angle of inclination on the equivalent value of thermal conductivity, thus allowing the material to be equally used in every part of the building envelope. Thus, polycarbonate has already found large usage, as in the Bavaria Brewery Tocancipá headquarters, by Construcciones Planificadas [41], where the plastic has been used to get an industrial appearance while providing for thermal and visual comfort, or the property registration offices, by Irisarri + Piñera, where polycarbonate has been used to complement and balance the appearance of the existing structure.

Across these materials already implemented in the traditional architectural paradigms, there is also a strong boost in the usage of plastics from the additive manufacturing (AM) sector, as several plastic products can also be utilized in AM processes, providing great freedom of form and enhancing designers', architects', and engineers' freedom in creating complex designs [42–46]. In addition, the global 3D printing filament material market volume was 1.8 billion US$ in 2019, growing at a compound annual growth rate (CAGR) of 27% [47]. The most popular filament materials are PolyLactic Acid (PLA) and Acrylonitrile-Butadiene-Styrene (ABS), holding about 47% and 29% of the market, respectively. In contrast, materials as PolyEthylene Terephthalate Glycol-modified (PETG) can be useful alternatives, despite not being as popular, providing similar mechanical properties while also offering excellent recyclability and scalability [47]. The AM in the facade industry presents new significant potential and requires relevant research to be conducted [46]. Indeed, more and more 3D printing materials are concurrently becoming utilized in contemporary architecture design [42–46], thanks to the lightness and effortless installation procedure, which results in a design solution useful for both new projects and refurbishment ones [44–46]. The 3D printing technology has been often used to create everything, from prototypes [42,43,46] and simple parts of facades, to give a distinctive signature to the constructions [44,45]. The 3D printing materials prove themselves to offer quite unique characteristics from an architectural and economic point of view [43–46]. Several scientific papers have been conducted into the loadbearing capacities and/or other essential qualities of AM products for the building industry, such as durability, water vapor diffusion resistance, thermal conductivity, or fire-resistance [48–51]. The authors emphasized the potential applications of additive manufacturing to build honeycomb panels that optimize mechanical properties and heat transfer [48–51]. However, scientific research related to 3D printing materials in building energy efficiency applications is limited due to its relatively new nature as a technology. Only Sarakinioti et al. [46] aimed their research at developing an integrated 3D printed for thermal insulation and building physics. In particular, they presented a 3D printed facade panel design for thermal insulation and movable liquid heat storage [46], providing an overview of the development process. The authors tested the prototype and, at the same time, simulated to verify the thermal effects of the proposed facade system on indoor spaces in different climates. The simulation results reported in [46] showed the potential of the proposed 3D printed facade panel for reducing heating and cooling energy demand. Therefore, the effects of adopting 3D printing materials as a second-skin layer on the indoor environment have been scarcely investigated.

Moreover, there is a lack of experimental testing and numerical model development of these materials in building simulation, even more, if considered in a second-skin in front of the building envelope, in a 3D printed composite facade arrangement. Indeed, in a facade arrangement realized with these innovative materials (ABS, PLA, PETG, etc.), the difficulties lie in predicting the behavior of the various facade sections, as the second-skin

layer, the resulting air cavity, and finally, the effects on the indoor environment. Therefore, from an experimental point of view, standardization bodies, experts, and researchers are continually developing new methodologies or new procedures to correctly calculate the performances of these envelope components in simple and economical ways [6].

1.2. Research Aims

In this work, extruded ABS panels have been tested as second-skin materials in order to verify their performances in an OVF system. This novel material for building envelopes has been investigated through in-situ measurements by using two outdoor comparative test cells. The experimental data have been used to calibrate and validate a numerical model in TRNSYS 18 [31], also verifying the ability of the simulation software to effectively reproduce the behavior of a light material in an OVF system, which usually is made of materials as porcelain gres. Then, the validated numerical methodology has been used to implement different plastic materials in a set of refurbishment case studies, compared to a reference office building, in order to assess the potential benefits. The comparison has been performed in terms of (i) heating and (ii) cooling energy demands, as well as (iii) non-renewable primary energy consumption, upon varying the plastic material. Finally, additional refurbishment case studies have also been implemented considering 3D printed panels as a second-skin layer.

The aims of this research can be summarized as reported below:

- investigate the performances of extruded ABS panels as a second-skin layer for innovative building envelopes with experimental tests in-situ;
- calibrate and validate a simulation model to predict the energy performance of the plastic and composite polymer panels used as a second-skin layer in an OVF system;
- assess the potential energy saving achievable in office building refurbishment using the proposed materials (extruded and 3D printed polymers) through numerical simulation.

1.3. Structure of the Research

The research is structured as follows.

Section 2 describes the methodology used to carry out the research, showing in detail how (i) the experimental data have been acquired, (ii) the numerical model has been implemented in TRNSYS 18, and how (iii) the experimental data have been used to calibrate and validate this numerical model.

Section 3 reports the numerical results, in terms of the reduction of non-renewable primary energy consumption, achieved in an office building refurbishment through the installation of an OVF system, upon varying the material used as a second-skin layer, considering both extruded and 3D printed ones.

Finally, Section 4 discusses the integration capacity of the plastic and composite polymer panels in a second-skin layer of an OVF system, highlighting the advantages and limitations of such materials.

2. Methodology

This section describes in detail the measurement methodologies and the experimental results obtained during the in-situ test as well as the methods and results related to the validation of the implemented numerical model.

2.1. Description of the Gemini Facilities, Experimental Results, and Discussion

In this sub-section, a couple of experimental test cells and the experimental results are reported. Gemini facilities [11] are designed and built at the Ri.A.S.–Built Environment Control Laboratory [52] of the Department of Architecture and Industrial Design of the University of Campania Luigi Vanvitelli in Aversa (40°59′39.1″ N, 14°10′48.5″ E). These full-size outdoor test cells have been designed to experimentally evaluate double-skin facade module performances, in real outdoor weather conditions. The test cells are designed as an identical couple in order to carry out comparative measurements. The Gemini's internal

dimensions are 2.20 m wide by 2.80 m deep and 2.40 m tall, oriented with the long side along the north-south axis. These dimensions correspond to the gross dimension of the main steel frame structure, on which the shell has been fixed externally and seamlessly in order to avoid thermal bridges. The shell has been realized in a single layer of 10 mm thick sandwich panels consisting of two galvanized steel sheets and a polyurethane rigid foam filling, with a thermal transmittance (U_{wall}) value of 0.23 W/m^{2}K [11]. Then, for the floor, a 0.10 m air gap and a wood flooring have been added above the structure, while, for the ceiling, a sheet metal roof has been placed 0.10 m above the outer panels, with a 2% slope, to allow a natural rainwater outflow.

The Gemini's facilities are designed to allow the in-situ characterization of innovative layers to be applied in double-skin facades with different geometries, layout, materials, and technologies. The acquired data can be used to evaluate the in-situ performances of the system under investigation and to realize, calibrate and validate simulation models.

The Gemini is well-instrumented to acquire different indoor and outdoor physical quantities. Table 1 shows the measurement range, the accuracy, and the response time of the sensors used for outdoor and indoor climate characterization. In particular, with the aim to evaluate the real weather conditions, sensors for wind direction, wind speed, air temperature, air relative humidity, air pressure, global horizontal radiation, and diffuse horizontal radiation were placed at about 6.50 m from the ground, in the best position to minimize the influence of external obstructions (i.e., the obstructions angles are less than 10°). In order to acquire diffuse horizontal radiation, one of the pyranometers is equipped with a shadow ring (diameter of 0.574 m and thickness equal to 0.052 m), and the data were corrected following the methodology proposed in [53], to take into account both the isotropic and anisotropic conditions. Figure 1 shows the weather station, with all the aforementioned sensors.

Table 1. Installed Gemini sensor measurement range and accuracy.

Number of Sensors	Measured Quantity	Type	Range	Accuracy
1	Wind speed	'Pro First Class' anemometer	0–50 m/s	±0.01 m/s
1	Wind direction	'Pro First Class' anemometer	0–356.9° ± 3°	±1°
3	Air Temperature and Relative humidity	Thermo-hygrometer with precision transducer	Temperature: −40–+60 °C Rel. Humidity: 0–100%	Temperature: ±0.2 °C Rel. Humidity: ±2%
1	Atmospheric pressure	Barometer with piezo-resistive transducer	800–1100 hPa	±0.3 hPa at 20 °C
3	Solar radiation	II class thermopile pyranometer	0–2000 W/m^2	±10 μV/(W/m^2)
2	Air cavity speed	Hot wire air speed transmitter	0.2–40.0 m/s	±0.2 m/s +3% f.s.
10	Temperature	T-Type thermocouple	−200–+350 °C	±1.5 °C

Figure 1. The weather station used to monitor the real outdoor conditions.

The air temperature inside the Gemini is monitored by a combined temperature-relative humidity sensor placed in the middle of the room. Also, when the test cells are configured to test a second-skin system, this is monitored through a set of ten thermocouples, placed on the significant interfaces and in the cavity.

The sensor layout follows the layout shown in Figure 2a. In particular, it can be noted that (i) six thermocouples are placed in the middle of both the inlet (T1, T2, and T3) and the outlet (T8, T9, and T10) sections of the air cavity, (ii) four thermocouples are placed in line at the center of the second-skin system (T4 on the back surface of the second-skin, T5 in the middle of the cavity, T6 on the external surface of the south wall of the test cell, T7 on the internal surface of the south wall of the test cell, respectively); this last set of thermocouples falls in line with the same thermo-hygrometer which monitors the temperature of the air inside the test cell, in order to have all the sensors aligned at the center of the system.

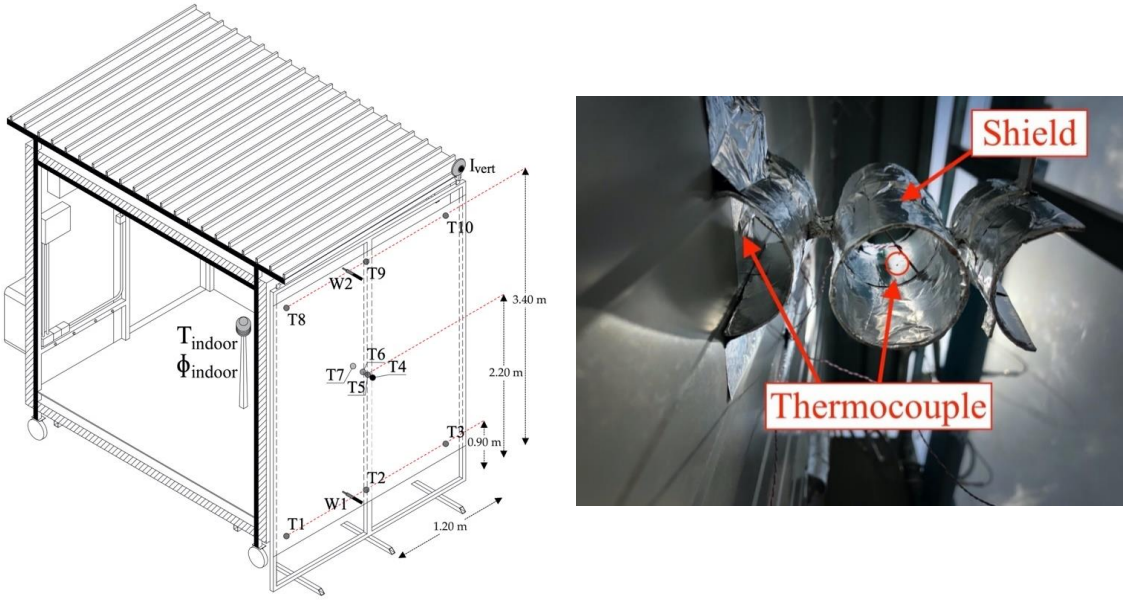

(**a**) (**b**)

Figure 2. (**a**) Axonometric views of the sensor layout; (**b**) shielding devices used in the experimental setup to avoid any direct solar radiation on the thermocouples.

In addition, all the thermocouples (Tx) have been shielded with high-reflective domes in order to avoid any direct solar radiation (Figure 2b).

The pyranometer (I_{vert}) has been installed to acquire the vertical solar radiation incident on the south surface and, finally, two hot-wire anemometers (W_{in}, and W_{out}) are placed in the air cavity, one in the inlet section and the other one in the outlet section, in order to monitor the airflow in the second-skin cavity.

In order to verify the measurement methodologies and characterize each test cell from the thermal point of view, preliminary data has been acquired in a standard configuration (both Gemini s without a second-skin system). These data are recorded with the aim of (i) verifying the operation of the different instruments and their correct positioning, (ii) comparing the thermal behavior of the two test cells, and (iii) defining a reference point for the following evaluation of the real performances of double-skin facades or smart windows. The preliminary experimental data were acquired and stored every 1 min on a period of 1 month (from 1 June to 30 June) and, later, averaged on an interval of 15 min. Figure 3 reports the indoor air temperature of Gemini 1 and Gemini 2, the external air temperature, and the global horizontal radiation for three typical days in June. This figure highlights that the difference between the indoor air temperature of Gemini 1 and the indoor air temperature of Gemini 2 ($T_{indoor,\ Gemini\ 1} - T_{indoor,\ Gemini\ 2}$) is negligible, varying within an interval with a maximum of 0.2 °C and a minimum of −0.2 °C.

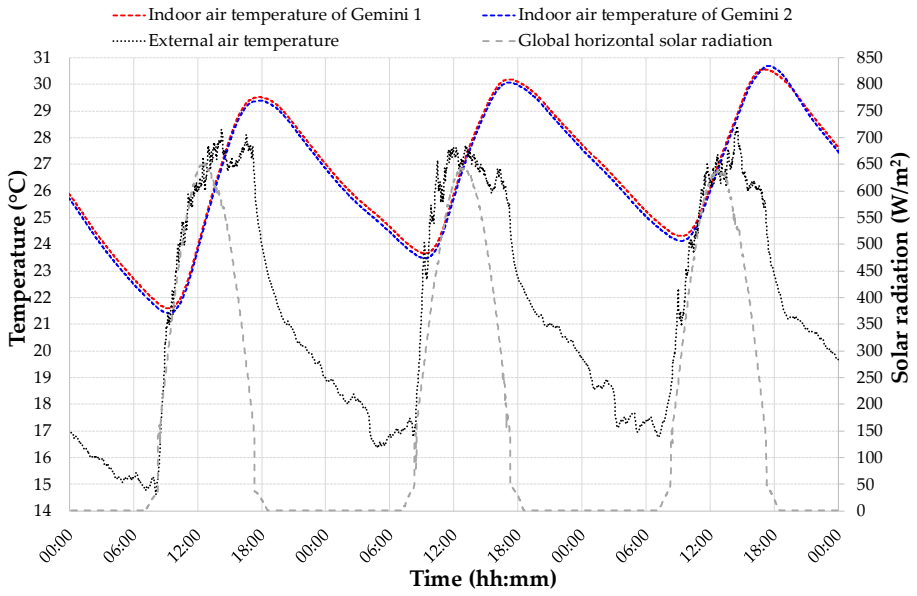

Figure 3. Gemini 1 and Gemini 2 preliminary experimental indoor air temperature trends for three typical June days.

After the preliminary experimental campaign, a second-skin system has been mounted and tested on a test cell (Gemini 1) with an air cavity gap equal to 0.10 m, while the other cell has been left unequipped and used as a reference (Gemini 2). In particular, the investigated second-skin system has been realized with extruded ABS panels [54]. The experimental data were acquired and stored every 1 min over a period of 1 month (from 8 December to 31 December) and, later, averaged on an interval of 15 min. This experimental campaign aims to verify the performances of plastic panels as a second-skin layer for innovative envelopes.

The extruded ABS panels have been selected with dimensions equal 600 mm × 1200 mm; such dimensions have been selected on the basis of the dimension of conventional panels in OVF systems, in order to guarantee an easy installation in a commercial OVF structure, as well as an easy substitution of conventional OVF system materials in a realistic scenario. In Figure 4a, a detailed view of the analyzed extruded ABS panel before the installation is

displayed, while Figure 4b shows the Gemini 1 equipped with the second-skin realized with six extruded ABS panels.

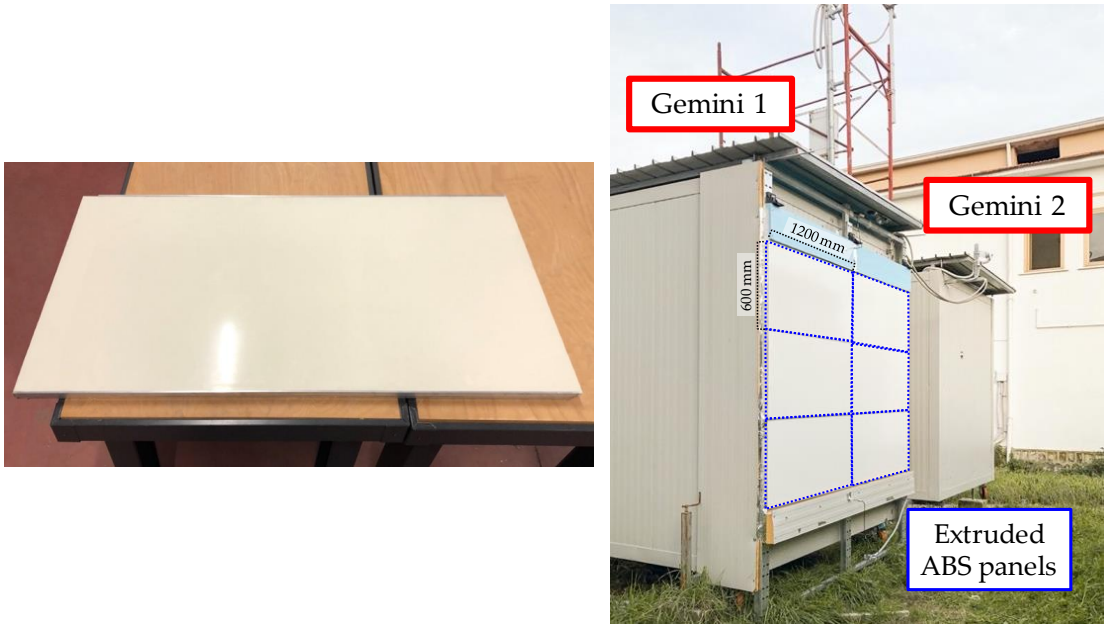

(**a**) (**b**)

Figure 4. (**a**) Extruded ABS panels [54] detail view; (**b**) Gemini 1 equipped with the OVF system.

The second-skin system equipped during the tests has been realized by mounting the six extruded ABS panels on a steel frame, then hanging the whole system to the brackets on the south facade of the test cell Gemini 1. Finally, the sides of the second-skin system were covered and sealed by means of panels, similar to those used for the test cells' envelope, in order to allow only for a vertical airflow in the cavity (Figure 4b). In this configuration, the acquisition period lasted for almost a month, in the wintertime. During the acquisition period, the temperatures were monitored following the layout reported in Figure 2a. Figure 5 shows an overview of the whole acquisition period, reporting the external air temperature, the global horizontal radiation, and the total vertical radiation on the south facade.

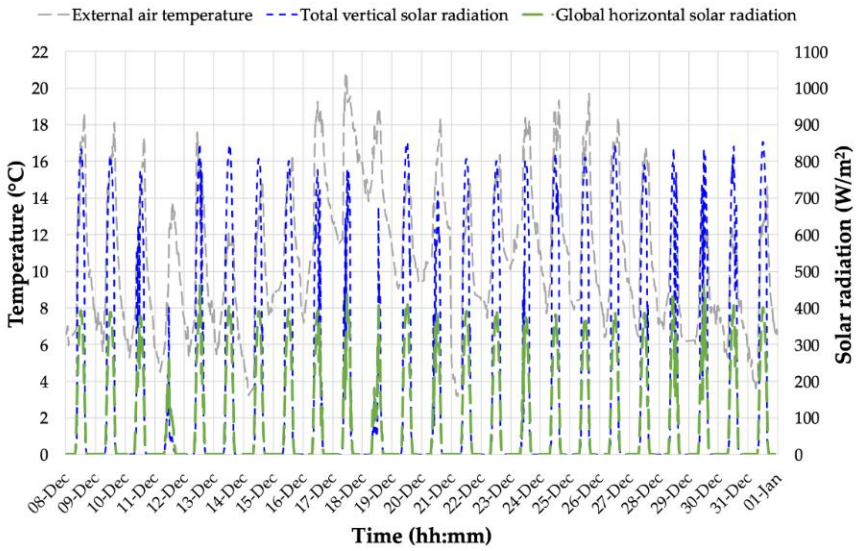

Figure 5. Overview of the whole winter acquisition period.

Figure 5 highlights that the external air temperature was quite warm, despite being the winter season. Also, the radiation values, both global horizontal and total vertical, show mostly high values, thus confirming good weather and clear sky across the whole acquisition period.

Figure 6a,b report a focus for four typical days on the weather conditions during the measurements with the Gemini 1 equipped with the second-skin system, and the Gemini 2 left uncovered as a reference. In particular, Figure 6a shows the temperature and solar radiation data (global horizontal solar radiation, diffuse horizontal solar radiation, and total vertical solar radiation on the south facade), while Figure 6b reports the wind characteristics acquired during the analyzed days; on the left axis the wind speed is reported, while on the right axis the wind direction is displayed, considering 0° as north direction, 90° as east direction, 180° as south direction, and 270° as west direction.

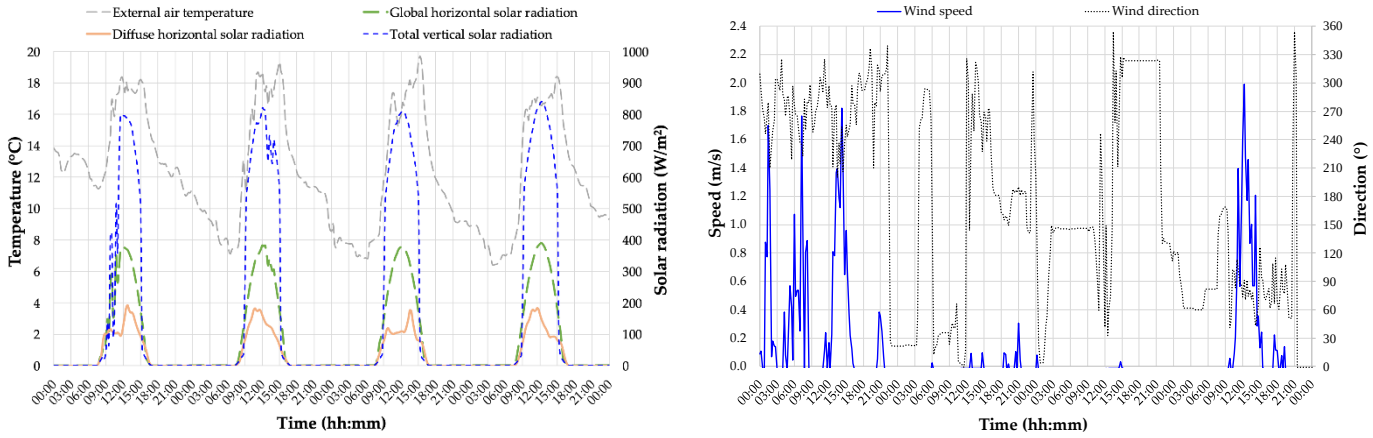

(**a**) (**b**)

Figure 6. Weather conditions during four typical acquisition days: (**a**) solar radiation and temperature; (**b**) wind speed and wind direction.

Figure 6a better highlights that, during the measurement period, sunshine days were acquired with atypical temperatures for the period, ranging between a minimum of about 5.9 °C and a maximum of about 19.4 °C.

Figure 6b shows a low wind speed in general during the measurement period and a slight wind predominance in the west/north-west direction. Also, the wind speed values acquired during the nighttime are equal to zero, due to a threshold value for the start/stop of the sensor equal to 0.15 m/s.

Figures 7 and 8 report the experimental data associated with the cavity with a 1-h timestep for a single acquisition day. In more detail, Figure 7 shows the trends of the daily values of the air temperature inside the cavity upon varying the height from the ground, while Figure 8 reports the airspeed at the inlet and the outlet of the air cavity, for the same day.

The data reported in Figure 7 corresponds to the measures of the three thermocouples positioned in the middle point of the cavity of the second-skin system, more specifically T2, in the middle of the air cavity inlet, T5, in the middle of the air cavity geometrical center, and T9, in the middle of the air cavity outlet, as shown in Figure 2a. As a first observation, the overall temperature distribution is directly related to solar radiation throughout the day, where the temperatures rise during the morning and drop during the afternoon. Also, during the day, the temperature trend seems to be substantially constant from the air cavity inlet to the middle of the facade, and then to increase to the air cavity outlet; this behavior is due to the chimney effect that is created thanks to the OVF system. Then, in the evening (starting from 16.00), the temperatures at the outlet of the cavity are only slightly higher than those at the center and the inlet; this is due to the reduction of solar radiation happening in the evening.

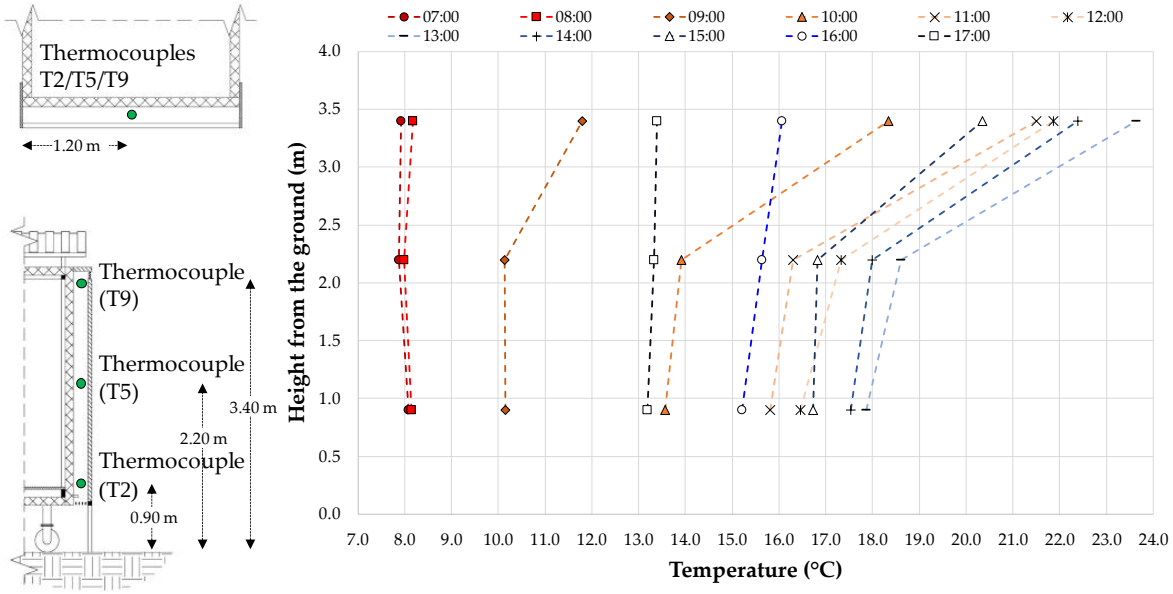

Figure 7. Daily values of the cavity air temperature.

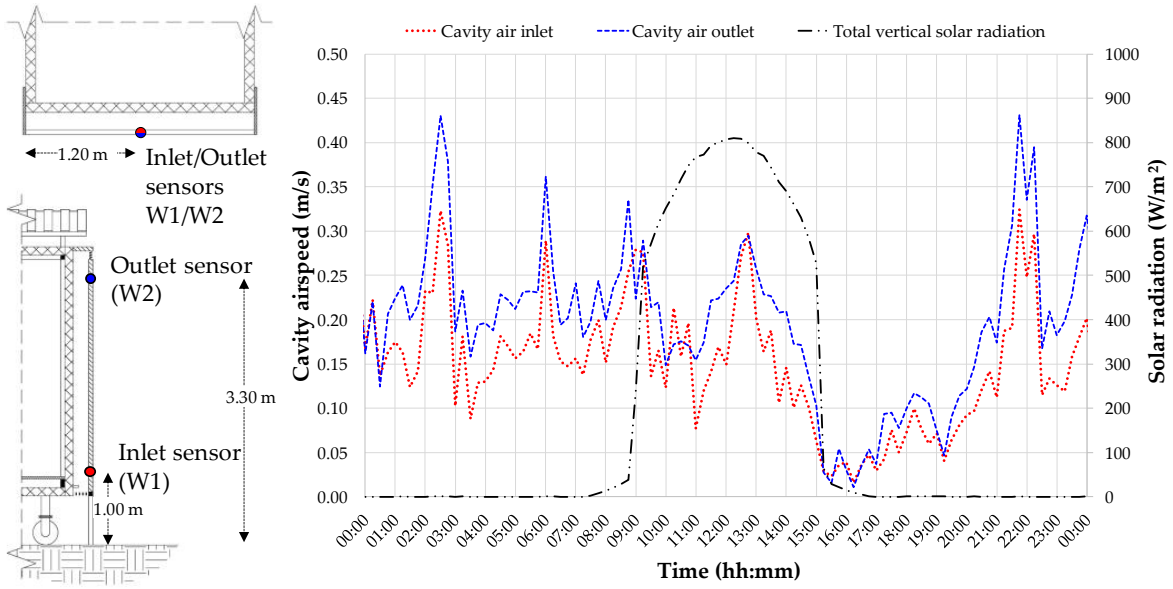

Figure 8. Daily values of the airspeed at the inlet and the outlet of the air cavity.

Figure 8 reports data acquired by the hot-wire anemometers placed based on the layout shown in Figure 2a, where W_{in} measured the airspeed value at the inlet of the cavity and W_{out} measured the value at the outlet of the cavity. This figure shows how, during the day, the values acquired by W_{out} is higher than those measured by W_{in}, referable to a direct effect of the solar radiation on the rising of the air temperatures along the air cavity, thus causing an increase in airspeed. After 15:00, the chimney effect in the air cavity is reduced because the temperatures are gradually decreasing over time due to the reduction of the solar radiation on the south facade; this causes a significant drop in the airspeed values measured in the cavity.

Therefore, the analysis of the experimental results shows that a plastic material (i.e., ABS) can be used as a second-skin layer in OVF systems.

2.2. Description of the Numerical Model

The software TRNSYS 18 [31] has been used to model the Gemini test cells and to develop the second-skin model. TRNSYS software adopts a modular approach by using Fortran subroutines. Each Fortran subroutine is called a 'Type' and contains the model for a single system component. Several studies have been carried out in order to validate the numerical models developed in TRNSYS from the Colorado State University experimental houses and other researchers around the world [55–58]. In this study, the following main TRNSYS Types [31,59–61] have been used:

- Type 56 to simulate the Gemini test cells [59];
- Type 1230 to model the second-skin system [61];
- Type 16c to estimate the solar radiation on the Gemini and second-skin system surfaces [59,60];
- Type 69b to determine the sky temperature [59,60];
- Type 33e to determine the moist air properties [59,60].

At first, the Type 56 subroutine has been used to model the thermal behavior of the Gemini test cells; in particular, two thermal zones have been modeled, one for each test cell. Also, Type 56 contains information about the test cells' surroundings (buildings, trees, bushes), which are described as 'shading objects'. The geometrical modeling occurred in the SketchUp software [62], where it was possible to model the shapes and the position of each element accurately. Then, by means of the Trnsys3D plug-in, the geometries were imported into the Type 56 subroutine. The physical properties of each test cell's external surface have been defined, on the basis of the data provided by the manufacturers. Lastly, the internal thermal gains have been set for each test cell, which was determined on the basis of the equipment installed inside the facilities (notebook, data acquisition systems, and uninterruptible power supply units).

The OVF system has been modeled using the Type 1230 subroutine, which effectively reproduces the behavior of an external second-skin layer with an air cavity behind it. Using this TRNSYS Type, the behavior of the OVF system has been correlated to that of the Gemini test cell modeled through the Type 56 subroutine. In particular, the last external layer of the Type 56 wall acts as an interface layer between the Type 1230 and the Type 56, by coupling its temperature and thermal resistance to model the wall heat transfer. Figure 9 shows a schematic of the boundaries of the two coupled Types (56 and 1230), highlighting the resistive interface layer. The Type 1230 parameters have been set following the data provided by the manufacturer of the extruded ABS panels [54], taking into account thickness, density, and thermal conductivity, specifically.

During the simulations, Type 1230 takes into account:

- the solar radiation, the longwave radiation, and the air convection on the external surface of the outside layer;
- the energy storage and the conduction in the outside layer;
- radiation exchange between the outside layer and the air cavity;
- the convective exchanges from all the surfaces facing in the air cavity;
- the conduction through the interface layer.

Type 16c has been implemented to model the solar radiation on all the external surfaces. This Type accepts global radiation, ambient temperature, and ambient relative humidity data as input, in order to output several quantities related to the position of the sun, as the diffuse radiation fraction on the horizontal, by estimating the cloudiness of the sky on the basis of the dry bulb temperature and the dew point temperature. Finally, the radiation on every external surface is computed, on the basis of their own orientation.

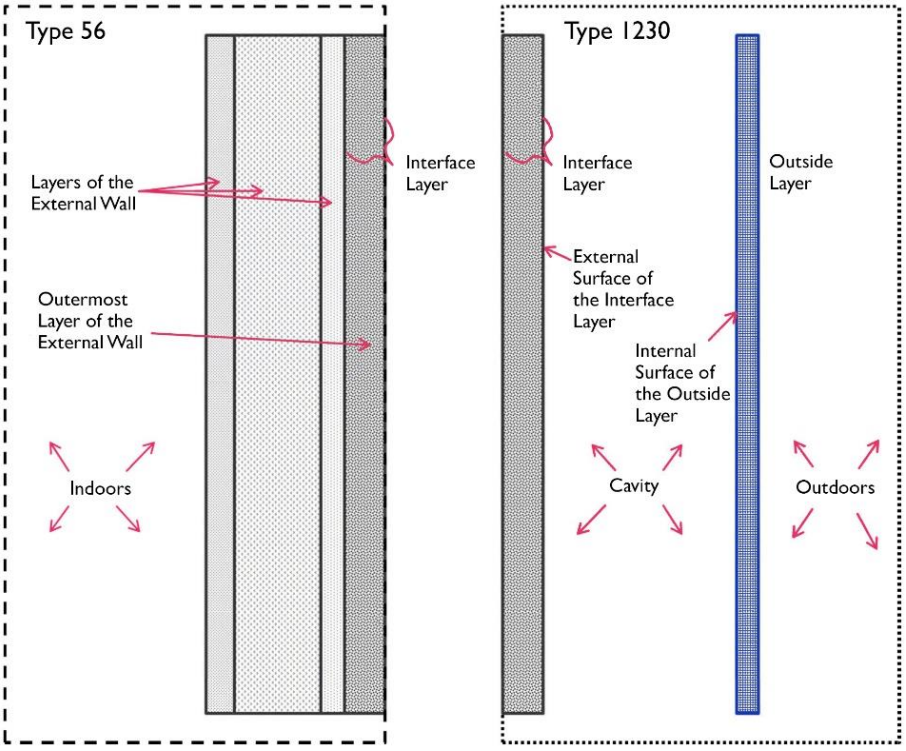

Figure 9. Coupling between Type 56 and Type 1230 [61].

The effective sky temperature is determined by means of Type 69b, which calculates the long-wave radiation exchanges between the external surfaces and the atmosphere. Type 69b calculates the cloudiness factor as well, on the basis of the dry bulb and the dew point temperatures.

Finally, Type 33e has been implemented in order to calculate the properties of the moist air, in particular, by taking the air temperature, the relative humidity, and the air pressure as input; it returns the density of the air mixture for every timestep, which is then used to calculate the airflow at the OVF inlet. In this way, the inlet airflow is not a fixed value, but it corresponds to the experimental data acquired through the hot wire anemometers, placed as reported in Figure 2a.

In this study, the experimental weather data acquired from 8 December to 31 December have been used as input data for the Type 16c, Type 69b, and Type 33e.

During the simulation, both the time base used to solve the differential equations and the simulation timestep has been set equal to 15 min in order to have a full correlation to the timestep of the experimental input data.

2.3. Validation of the Numerical Model

This sub-section reports the methods and results related to the validation of the numerical model. The model reliability has been verified in terms of indoor air temperature (T_{indoor}) and the average temperature of the air cavity (T_{cavity}) by comparing the experimental values with those obtained as an output of the simulation model above described, defining the following percentage differences ΔT_{indoor} and ΔT_{cavity}:

$$\Delta T_{indoor} = \left(T_{indoor,exp} - T_{indoor,sim}\right) / T_{indoor,exp} \quad (1)$$

$$\Delta T_{cavity} = \left(T_{cavity,exp} - T_{cavity,sim}\right) / T_{cavity,exp} \quad (2)$$

Figure 10a,b report the comparison between the simulation results and the experimental data acquired during the whole test period (from 8 December to 31 December) in terms of T_{indoor} and T_{cavity}, respectively.

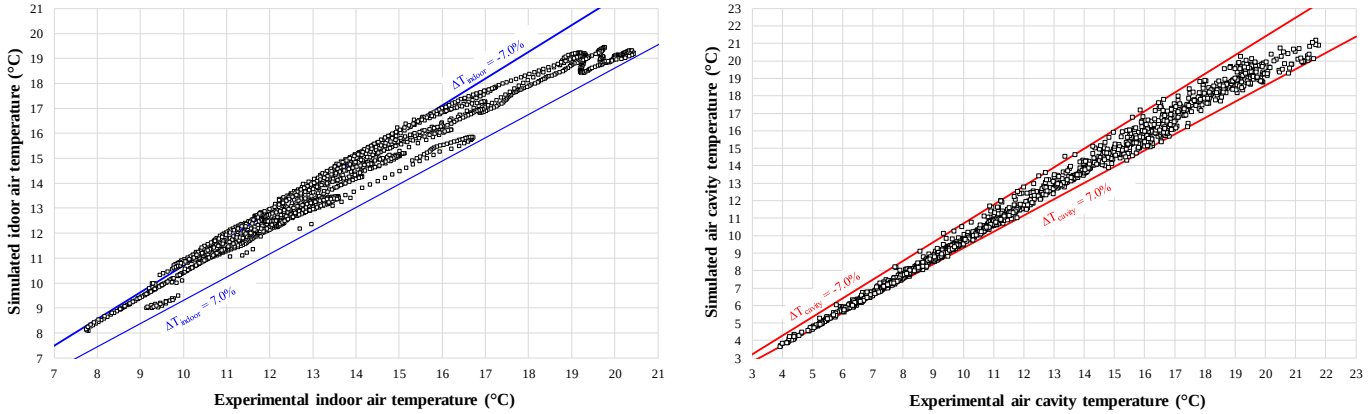

(**a**) (**b**)

Figure 10. Comparison between the simulated values and the experimental values acquired during the whole test period in terms of (**a**) T_{indoor} and (**b**) T_{cavity}.

These figures highlight how the developed model is quite reliable, with values of ΔT_{indoor} ranging between a minimum of −9.62%, and a maximum of 6.22%, as well as the values of ΔT_{cavity} between a minimum of −8.51% and a maximum of 7.85%.

The accuracy of the model has also been validated by calculating the mean error (*ME*), the mean absolute error (*MAE*), and the root mean square error (*RMSE*) as reported below:

$$ME = \sum_{i=1}^{N} (T_{\exp,i} - T_{sim,i}) / N \quad (3)$$

$$MAE = \sum_{i=1}^{N} \left| T_{\exp,i} - T_{sim,i} \right| / N \quad (4)$$

$$RMSE = \sqrt{\sum_{i=1}^{N} \left((T_{\exp,i} - T_{sim,i}) - ME \right)^2 / N} \quad (5)$$

where $T_{exp,i}$ is the experimental value at time step i, $T_{sim,i}$ is the simulated value at time step i, and N is the number of measurements. Table 2 reports the values of the *ME*, *MAE*, and *RMSE* for both T_{indoor} and T_{cavity}.

Table 2. Values of *ME*, *MAE*, and *RMSE* obtained by comparing the simulated values and the experimental data acquired during the whole test period.

T_{indoor} (°C)			T_{cavity} (°C)		
ME	*MAE*	*RMSE*	*ME*	*MAE*	*RMSE*
−0.3	0.5	0.4	0.3	0.3	0.2

The values reported in Table 2 highlight that there is a slight difference between the measured and predicted results, in particular: (i) the ME associated to the T_{indoor} is equal to −0.3 °C, which means that the simulation model slightly overestimates the indoor air temperature, while that associated to the T_{cavity} is equal to 0.3 °C; (ii) the values of RMSE are equal to 0.4 °C and 0.2 °C for T_{indoor} and T_{cavity}, respectively.

Therefore, the results show the ability of the Type 1230 to accurately predict the behavior of the extruded ABS panels in an OVF system. Thus, the same methodology is used to carry out a complete numerical campaign on a set of case studies upon varying the polymer (selecting the ones more used in architecture, as highlighted in the literature review) and manufacturing technology (extruded and 3D printed).

3. Materials and Numerical Modeling Implementation

The software TRNSYS 18 [24] is used to assess the potential energy saving achievable in an office building refurbishment using plastic and composite polymers as the second-skin layer material.

The office building modeled in this work is the same for all configurations and it consists of three identical floors. Each floor has a surface of 451 m^2 and a volume equal to 1503 m^3, with a total window area ($A_{w,\,total}$) of 112.3 m^2 ($A_{w,\,North}$ = 24.5 m^2, $A_{w,\,South}$ = 87.8 m^2). It is located in Napoli (latitude = 40°51′ N; longitude = 14°16′ E), and as such, in order to simulate the weather condition, the corresponding EnergyPlus weather data has been used [30]. The office is firstly modeled in the SketchUp 3D modeling software (Figure 11). Then, the 3D model geometries were exported by means of the Trnsys3D plug-in and successively imported into TRNSYS 18 in order to model the building envelope (stratigraphy of the opaque wall and window typology), to define the infiltration, the internal gains, the operation period of the heating and cooling systems as well as the operation of the electric equipment and lighting system. In particular, the same TRNSYS Types described in Section 4 have been used to simulate the case study.

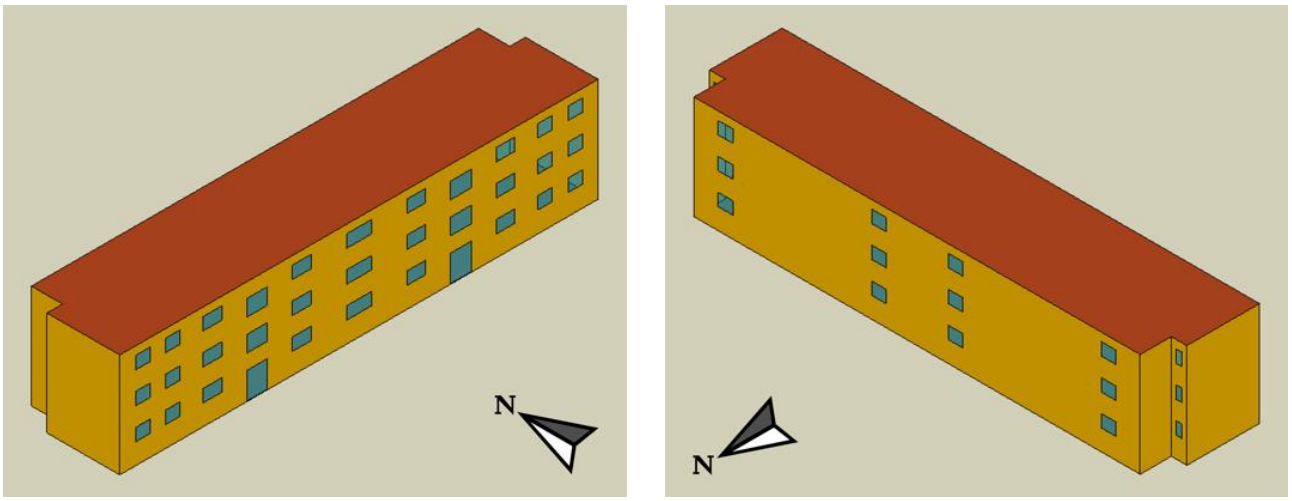

Figure 11. Office building modeled in SketchUp 3D: (**a**) south view; (**b**) north view.

The same typical three-story office building is investigated upon, varying the insulation layer thickness on the south facade and the typology of second-skin material, for a total of eight case studies. Table 3 summarizes the eight simulation cases investigated in this work. In particular, this table reports the reference case (Case 0) without the second-skin (Figure 12a) and seven refurbishment case studies with the OVF system (Figure 12b) upon varying the second-skin material. These cases are:

- Case 1, with an OVF system made of a conventional second-skin material (Porcelain gres);
- Cases 2–5, where the OVF systems have been implemented by using the extrude plastic and polymer materials more used in architecture (polycarbonate multi-wall sheets, ABS, PETG, and PLA);
- Cases 3_3D–5_3D, where the second-skin materials used in the OVF are the most popular 3D printed polymers (ABS, PETG, and PLA);

Table 3. Summary of case studies investigated.

Case Study	Second-Skin Material	Insulation Thickness (m)	Air Gap (m)
Case 0	-	-	-
Case 1	Porcelain gres	0.072	0.10
Case 2	Polycarbonate multi-wall sheets	0.063	
Case 3	Extruded ABS panels	0.070	
Case 4	Extruded PETG panels	0.071	
Case 5	Extruded PLA panels	0.069	
Case 3_3D	3D printed ABS panels	0.065	
Case 4_3D	3D printed PETG panels	0.067	
Case 5_3D	3D printed PLA panels	0.063	

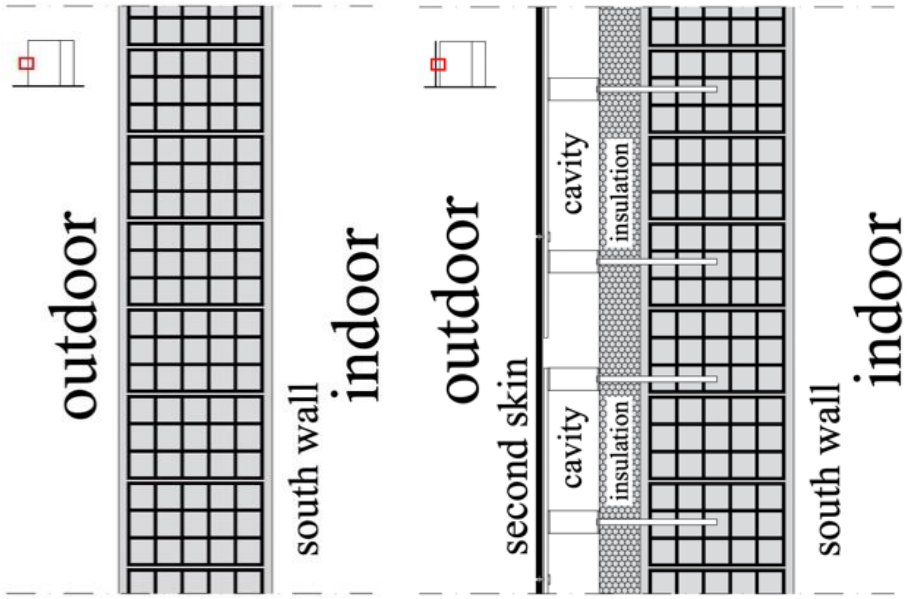

Figure 12. Section of the south wall of the office building: (**a**) reference case; (**b**) retrofit cases with the second-skin system.

In addition, an insulation layer has been added in each case study in order to reach the threshold values specified by the Italian Law [63] and equal to 0.36 W/m^{2}K for the climatic zone considered in this work. The different insulation thicknesses are also reported in Table 3, upon varying the simulation case.

In all the retrofit cases, the cavity inlet airspeed is directly related to the wind speed and direction, as only the wind coming from a similar orientation as the second-skin system (wind direction = 180° ± 45°) has been considered as input for the Type 1230. In addition, the second-skin system has a control logic for the air cavity shutters, which are considered open during the cooling period and closed during the heating period.

Table 4 shows the thermal-physical properties of the opaque walls of the envelope implemented in the case studies.

Table 4. Thermal-physical properties of the opaque walls implemented in the reference case study.

Surface	Material	Thickness (m)	Density (kg/m^3)	Thermal Conductivity (W/mK)	Thermal Capacity (kJ/kgK)
Vertical Walls	Plaster	0.015	1400	0.70	1.01
	Bricks	0.238	600	0.36	0.84
	Mortar	0.015	1800	0.90	0.91
Roof	Plaster	0.015	1400	0.70	1.01
	Lighter concrete	0.027	500	0.17	0.88
	Bricks	0.150	600	0.36	0.84
	Concrete	0.020	600	0.18	0.88
	Bitumen	0.005	1200	0.17	1.47
Floor	Tiles	0.020	2000	1.00	1.00
	Concrete	0.050	600	0.18	0.88
	Bricks	0.150	600	0.36	0.84
	Lighter concrete	0.030	500	0.17	0.88

Table 5 reports the general simulation parameters adopted in the eight different case studies. In particular, this table highlights: (i) the values of the thermal transmittance for both opaque walls and windows, (ii) the air infiltration rate, (iii) the target of the indoor air temperature, the operation period, and the characteristics of the heating and cooling system, (iv) the occupancy schedule and (v) the internal gains. As can be noticed from Table 5, in all the retrofit cases the values of thermal transmittance for the opaque surfaces are equal to those of the reference case (Case 0), with the exception of the south wall, where the OVFs have been implemented and the thermal transmittance has been set equal to the threshold values specified by Italian law [63], considering the second-skin materials, the air cavity and the insulation thicknesses reported in Table 3.

Two parallel-connected electric heat pump (EHP) devices, model CRA/K 91 [64], coupled with a multi-split type air conditioning system, have been used to cover both the heating and cooling demands. The national grid has been used to cover all the electrical energy demand.

The simulation timestep has been set to 30 min.

Finally, Type 1230 [61] has been used to model a second-skin layer in plastic and composite polymers. The parameters required by Type 1230 for each material (i.e., density, thermal capacity, and thermal conductivity), for Cases 1–5, have been derived on the basis of the manufacturers or literature data [40,54,65–67]. With respect to the 3D printed panels (Cases 3_3D–5_3D), several specimens have been printed (Figure 13), in order to measure the final dimensions and density.

(**a**) (**b**) (**c**)

Figure 13. The specimens made through the 3D printing process: (**a**) ABS [68]; (**b**) PETG [69]; (**c**) PLA [70].

The thermal conductivity of the 3D printed materials (k_{3D}) has been calculated by means of the equation expressed by [48,51] and reported below:

$$k_{3D} = k_m \times \frac{2 \times \left(\frac{k_d}{k_m} - \frac{k_d}{a \times h_c} - 1\right) \times V_d + \frac{k_d}{k_m} + \frac{2 \times k_d}{a \times h_c} + 2}{\left(1 - \frac{k_d}{k_m} - \frac{k_d}{a \times h_c}\right) \times V_d + \frac{k_d}{k_m} + \frac{2 \times k_d}{a \times h_c} + 2} \quad (6)$$

where k_m is the thermal conductivity of the polymer as declared by their manufacturers [68–70], k_d is the thermal conductivity of the filler consisting of the air in the hexagonal cavities of the printed panels (equal to 0.026 W/mK [71]), a is the filler radius measured from the specimens (measured as 0.0045 m), h_c is the interfacial boundary conductance (considered equal to 12 W/m^{2}K [48]) and V_d is the volume fraction of the filler in the polymer matrix (calculated as 0.69 of the specimens' total volume). The internal geometries have been modeled as hexagons as suggested by [50], where hexagons specimens resulted as the most resilient to physical stress, thus more suitable for a building envelope integration.

Table 5. Simulation parameters used in this research.

Parameter	Detail	Value
Thermal Transmittance	Walls and South wall without insulation (Case 0)	U = 1.15 W/m^{2}K
	Roof	U = 1.10 W/m^{2}K
	Floor	U = 0.94 W/m^{2}K
	Windows (frame ratio of 15%)	U = 2.95 W/m^{2}K
	South wall with insulation (Cases 1, 2, 3, 4, 5, 3_3D, 4_3D and 5_3D)	U = 0.36 W/m^{2}K
Infiltration [72,73]	Air changes per hour	0.6 h^{-1}
Heating and Cooling systems	Heating system	Set point = 20 °C [74] Operation period = 16 November/30 March [74] COP = 2.67 [64]
	Cooling system	Set point = 26 °C [74] Operation period = 1 April/15 November [74] EER = 2.41 [64]
Occupancy schedule [75]	Workweek	Weekdays (8:00–18:00) Completely off on the weekends
Internal gains [76]	Lighting systems	Operation = Occupancy schedule Radiative = 11.13 W/m^2 Convective = 4.77 W/m^2
	Equipment	Operation = Occupancy schedule Radiative = 1.4 W/m^2 Convective = 5.6 W/m^2
	Occupants	Operation = Occupancy schedule Radiative/Convective = 2.5 W/m^2 Absolute humidity = 0.0055 kg/hm^2

Table 6 reports the parameters used to simulate the second-skin systems in the retrofit cases.

Table 6. Summary of the main simulation parameters for the Type 1230, upon varying the materials used as a second-skin layer.

Parameters	**Case 1**	**Case 2**	**Case 3**	**Case 4**	**Case 5**	**Case 3_3D**	**Case 4_3D**	**Case 5_3D**
Material	Porcelain gres	Polycarbonate multi-wall sheets	Extruded ABS	Extruded PETG	Extruded PLA	3D printed ABS	3D printed PETG	3D printed PLA
Thickness (m)	0.010							
Density (kg/m^3)	2000	300	1040	1300	1300	331	411	395
Thermal capacity (kJ/kgK)	0.840	1.05	1.40	1.20	1.80	1.21	1.07	1.25
Thermal conductivity (W/mK)	1.20	0.0453	0.17	0.29	0.13	0.0548	0.0818	0.0448
Resistance of interface layer (hm^2K/kJ)	0.486	0.427	0.472	0.479	0.467	0.438	0.455	0.427
Convective heat transfer coefficient of interface layer (kJ/hm^2K)	2.06	2.34	2.12	2.09	2.14	2.28	2.20	2.35

In conclusion, two additional parameters have been set for each case study, required by the Type 1230 as highlighted in Section 4: the resistance of interface layer, to be set in Type 1230 itself, and the convective heat transfer coefficient of the interface layer, to be set in the construction south wall in Type 56 instead. The convective heat transfer coefficients of the back of the south wall value have been set equal to the thermal transmittance value of the insulation layers, which act as interface layers between the two TRNSYS Types, while the thermal resistance values of the interface layer have been simply calculated as the inverse of the convective heat transfer coefficients.

These plastic and polymer materials do not differ only in terms of thermo-physical properties but also in terms of cost. In this work, the capital cost for each retrofit action has been neglected; however, Table 7 provides an overview of the costs per square meter associated with each plastic and polymer material implemented as a second-skin layer in the OVF system [54,77–79]. In general, the polycarbonate multi-wall sheets prove to be the cheaper material (10–25 €/m^2), being also the only one which is already used in the building sector; instead, the 3D printed panels are the more expensive ones (188–225 €/m^2). This cost limitation is typical for the 3D printing technology, especially compared to more traditional building materials. Despite this significant difference in cost, it must be noted that 3D printing is an emerging technology which usage is still not so widespread. However, the 3D printing technology is the only one that would allow for the obtaining of complex panels' shapes easily. Also, the price of the 3D printed panels reported in Table 7 are related to the brand-new spool, while it is possible to integrate also recycled filament spools in the production process [47]; indeed, the 3D printing manufacturing process is the only one where it's easy to fully integrate eco-compatible materials, like PLA.

Table 7. Costs per square meter of plastic and polymer materials used as a second-skin layer in this research [54,77–79].

	Polycarbonate Multi-Wall Sheets	Extruded ABS	Extruded PETG	Extruded PLA	3D Printed ABS *	3D Printed PETG *	3D Printed PLA *
Cost (€/m^2)	10–25	70–175	75–150	75–130	188–225	190–220	190–207

* Considering about 3.2 kg of material and including also the 3D printing cost (equal to 1.0 €/h, for 130 h of the whole printing process), for a panel of 1 m^2.

3.1. Energy Analyses: Methods

According to [12,75], the energy comparison between the proposed case (PC) and the reference case (RC) has been carried out considering the non-renewable primary energy consumption through the index PES (non-renewable primary energy saving):

$$PES = \left[\left(E_p^{RC} - E_p^{PC}\right)/E_p^{RC}\right] \times 100 \quad (7)$$

where E_p^{RC} is the non-renewable primary energy associated with the reference case (Case 0, see Table 3), while E_p^{PC} is the non-renewable primary energy associated with the eight proposed cases (Cases 1–5 and Cases 3_3D–5_3D, see Table 3).

The values of the E_p^{RC} and E_p^{PC} are calculated as reported below:

$$E_p^{RC} = \left(\frac{E_{th}^{RC}}{COP} + \frac{E_{cool}^{RC}}{EER} + E_{el,equipment} + E_{el,lighting}\right)/\eta_{PP} \quad (8)$$

$$E_p^{PC} = \left(\frac{E_{th}^{PC}}{COP} + \frac{E_{cool}^{PC}}{EER} + E_{el,equipment} + E_{el,lighting}\right)/\eta_{PP} \quad (9)$$

where η_{PP} is the Italian power plants' average efficiency, including the transmission losses, and it is assumed equal to 0.42 [74].

A positive value of the index PES means that the proposed refurbishment allows reducing the non-renewable primary energy consumption with respect to the reference case.

3.2. Energy Analyses: Results

In this section, the simulation results of the refurbishment case study are reported and commented on.

Figure 14 reports the values of PES as a function of the proposed case studies, while Figures 15 and 16 show the main energy flows of the building during the whole simulation period upon varying the simulation case. In particular, Figures 15 and 16 report the thermal energy flows in positive values, while the cooling energy flows in negative values.

These figures highlight that:

- all the proposed OVF systems return positive PES values in comparison to the reference case, which means a reduction of the non-renewable primary energy consumption ranging from 2.58% (Case 1) and 2.64% (Cases 2 and 5_3D); this is due to an average reduction of the thermal and cooling energy demands of about 6.9% and 3.0%, respectively;
- the retrofit actions where the plastic and composite polymers materials are used as a second-skin layer (Cases 2–5 and Cases 3_3D–5_5D, see Table 3) allow for a slight performance improvement with respect to those realized with a conventional second-skin material (Case 1), thanks to a reduction in the space cooling energy demand ranging from 31 kWh (Case 4) and 120 kWh (Case 5_3D);
- the results associated with the polycarbonate multi-wall sheets (Case 2) show a behavior similar to the Cases 3_3D–5_5D, mostly due to the fact that the polycarbonate panels have a structure assimilable to the 3D printing logic;

- considering the cases with the same polymers (Case 3 vs. Case 3_3D, Case 4 vs. Case 4_3D, and Case 5 vs. Case 5_3D), the 3D printed panels allow for a slight improvement in performances.

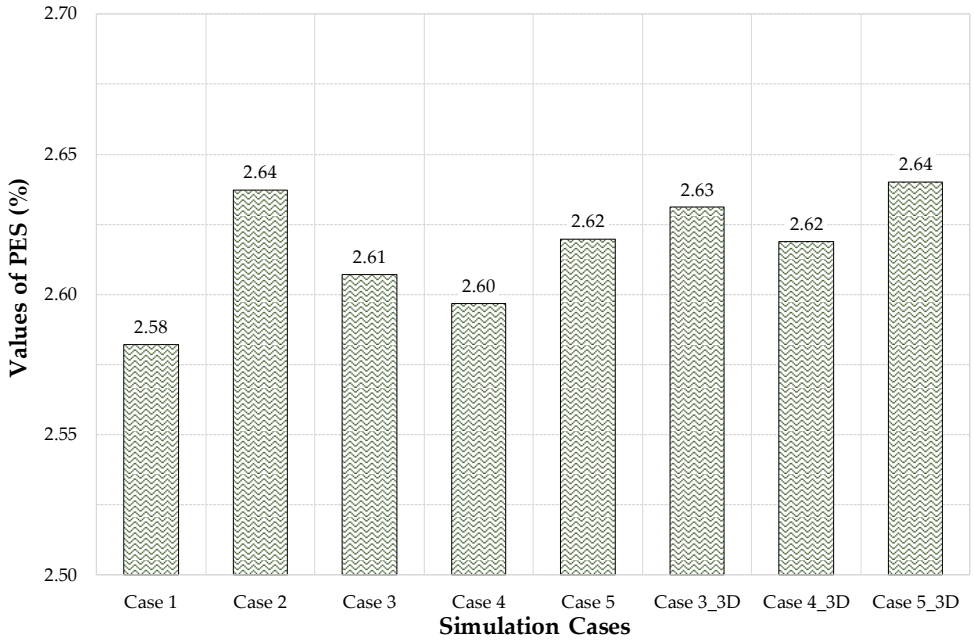

Figure 14. Values of PES upon varying the case studies.

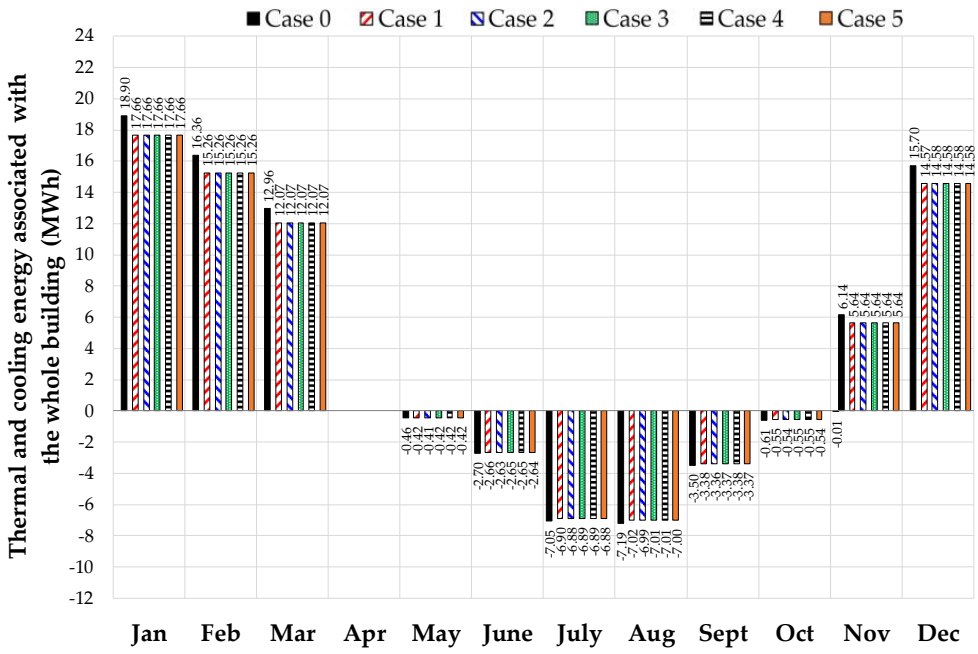

Figure 15. Main energy flows of the building during the whole simulation period associated with Case 0, Case 1, and retrofit Cases with extruded panels.

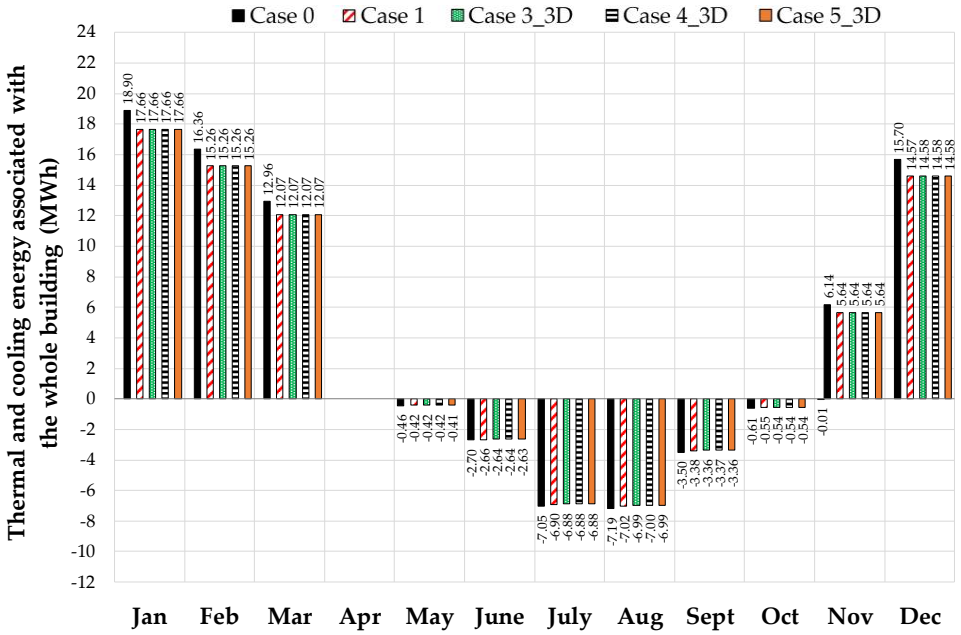

Figure 16. Main energy flows of the building during the whole simulation period associated with Case 0, Case 1, and retrofit Cases with 3D printed panels.

In order to better investigate the performance of the plastic and polymer materials used as a second-skin layer in the proposed OVF system, the trends of the values of the air temperature inside the cavity and the airspeed at the inlet and the outlet of the air cavity for the Case 5_3D in a typical summer day (2 August) is also reported in Figures 17 and 18 with a 1 h timestep. In general, similar trends in the values of the temperatures in the cavity as well as the airspeed at the cavity inlet and the outlet have been predicted for all the other cases.

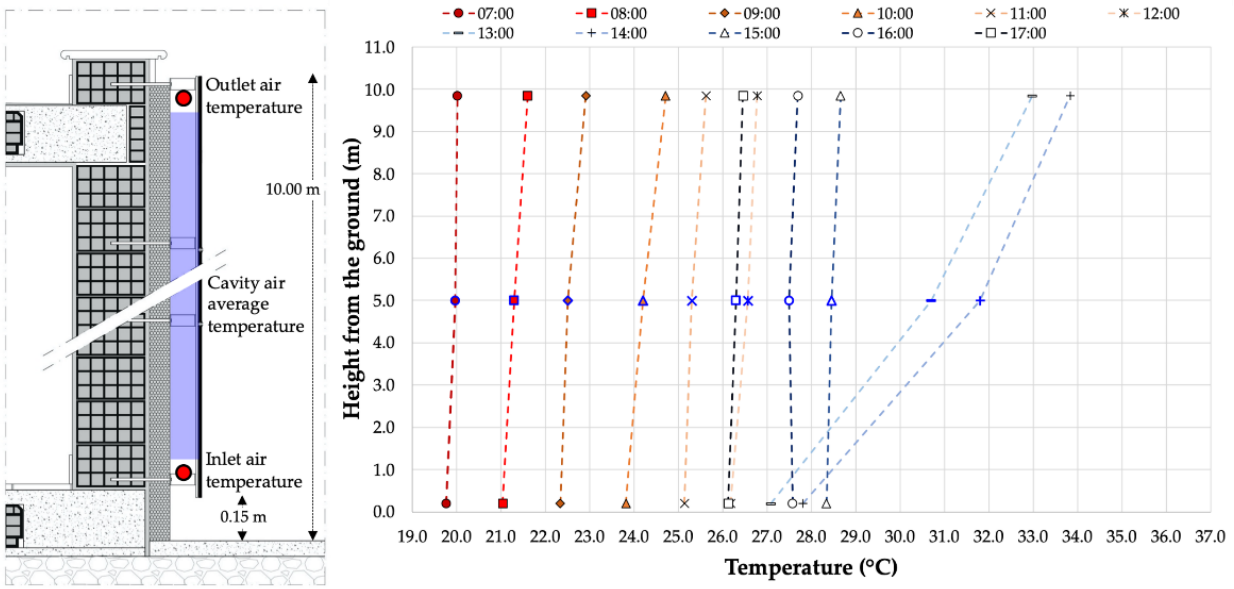

Figure 17. Simulated daily values of the cavity air temperature for a typical summer day.

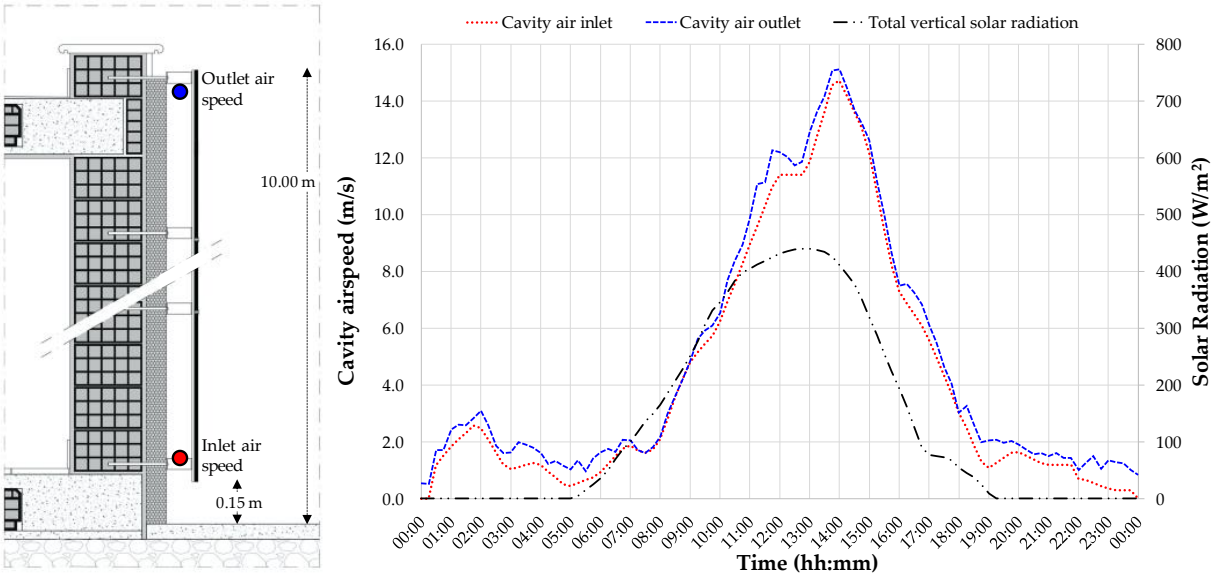

Figure 18. Simulated values of the airspeed at the inlet and the outlet of the air cavity for a typical summer day.

In more detail, Figure 17 shows the trends of the daily values of the air temperature inside the cavity upon varying the height from the ground, and, in particular reports, the temperature of the air at the cavity inlet (about 0.15 m from the ground), the average temperature of the air cavity (highlighted by the blue region in the building section) and the temperature of the air at the cavity outlet (about 10.00 m from the ground); Figure 18 reports the values of the airspeed at the cavity inlet (about 0.15 m from the ground) and the airspeed at the cavity outlet (about 10.00 m from the ground), as well as the total vertical radiation on the external surface of the second-skin layer.

The data reported in Figure 17 corresponds to the input and outputs of Type 1230. In particular, the inlet air temperature is an input for Type 1230, while the average air temperature in the whole cavity (T_{cavity}, the blue-edged markers in Figure 17) and the outlet air temperature are returned as output results by Type 1230 itself. These values represent the only two temperature values associated with the air cavity returned by Type 1230 [61]. As a first observation, the overall temperature distribution is directly related to solar radiation throughout the day, where the temperatures rise during the morning and drop during the afternoon. Also, during the day, the temperature trend seems to be constantly rising from the air cavity inlet to the air cavity outlet; this behavior is due to the chimney effect that is created thanks to the OVF system.

Figure 18 reports the simulation data corresponding to the cavity inlet airspeed (input of the Type 1230) and the cavity outlet airspeed (output of the Type 1230), as well as the total vertical solar radiation. This figure shows how, during the day, the values predicted at the cavity air outlet are always higher than those at the cavity air inlet (with a difference between outlet and inlet ranging from 0.01 m/s and 1.46 m/s), gradually rising to a maximum peak at around 14:00.

Finally, in order to verify the potential benefits coming from the best case, an additional simulation case, not reported in Table 3, has been carried out. In this last simulation, the OVF system has been implemented on the whole building, following the same installation methodology of the previous cases. The material selected as a second-skin layer is the 3D printed PLA, which proved to be one of the most effective in improving the non-renewable primary energy saving. The proposed OVF system returned a PES value equal to 8.10% if compared to the reference case.

4. Conclusions

The OVFs have been, more and more frequently, chosen for different building typologies (offices, schools, residential) and in different climates. Nowadays, there are always more innovative materials used in architecture and as a second-skin layer, even if the evaluation of their impact on the envelope's energy performance is a complex task. In particular, the use of polymers in building and engineering has increased substantially, thanks to their: (i) ease of production, (ii) ease of installation, (iii) durability, (iv) low maintenance requirements, (v) lightweight nature and (vi) ability to be formed into complex shapes. Several of these plastic products can also be utilized in additive manufacturing processes, providing excellent freedom of form, enhancing designers, architects, and engineers' freedom in creating complex designs.

In this work, the numerical model of extruded ABS panels in an OVF system has been developed and validated. Then, the simulation methods, suggested by the authors, have been applied in different refurbishment cases upon varying: the polymer and the manufacturing technology, extrusion (polycarbonate multi-wall sheets, ABS, PETG, and PLA), and 3D printing (ABS, PETG, and PLA).

The simulations have been carried out in order to assess the potential benefits achievable in terms of non-renewable primary energy saving, as well as thermal and cooling energy demand reduction. The simulation results highlight that: (i) all the proposed retrofit cases allow to achieve a benefit in terms of PES; (ii) the plastic and composite polymers materials allow for a slight performance improvement with respect to conventional second-skin material, such as porcelain gres; (iii) the best performances among the extruded polymers are returned by the polycarbonate multi-wall sheets (PES value equal to 2.64%); (iv) the best performances among the 3D printed polymers are achieved when using the PLA (PES value equal to 2.64%). However, the polymers' results show very similar performances, thus allowing building contractors, designers, and architects to select the material based on other project requirements, as mechanical strength, weather resistance, environmental impact, etc.

In this work, the thermal conductivity of the 3D printed materials has been calculated by means of an equation expressed in literature; therefore, in order to improve the accuracy of the model for the 3D printed material, in future works, the authors will carry out experimental investigations on full-scale 3D printed panels in OVF systems through the Gemini test cells. In addition, the capital cost for each retrofit action has been neglected. However, they represent an important parameter in the refurbishment typology choice; therefore, in future work, the authors will focus on a detailed economic analysis considering both the operating cost reduction and the simple payback period.

Author Contributions: Conceptualization, G.C., Y.S., M.S., A.R., and S.S.; methodology, G.C., Y.S., M.S., A.R., and S.S.; software, G.C. and Y.S.; validation, G.C., Y.S., M.S., A.R., and S.S.; formal analysis, G.C., Y.S., M.S., and A.R.; investigation, G.C. and Y.S.; resources, G.C. and S.S.; data curation, G.C. and Y.S.; writing—original draft preparation, G.C., Y.S., and S.S.; writing—review & editing, G.C., Y.S., M.S., and A.R.; visualization, G.C., Y.S., M.S., A.R., and S.S.; supervision, G.C., M.S., and S.S.; project administration, G.C., M.S., and S.S.; funding acquisition, S.S. All authors have read and agreed to the published version of the manuscript.

Funding: This research was co-funded by a collaborative research and development project, number F/050405/01-03/X32 "WALLED: Smart LED&OLED per Lighting e MediaBuilding"–Fondo per la crescita sostenibile–Call Horizon 2020 PON I&C and by the European Union-PON for Research and Innovation 2014–2020.

Data Availability Statement: The data presented in this study are available on request from the corresponding authors.

Acknowledgments: The authors would like to thank the Academic Editors for their invitation to the Special Issue "Novel Technologies to Enhance Energy Performance and Indoor Environmental Quality of Buildings" and the Assistant Editor for his support. The authors would also like to thank the three anonymous reviewers for their insightful suggestions and careful reading of the manuscript.

Conflicts of Interest: The authors declare no conflict of interest.

Nomenclature

Latin letters	
A	surface area (m^2)
a	filler radius (m)
ABS	acrylonitrile-butadiene-styrene
AM	additive manufacturing
$CAGR$	compound annual growth rate
COP	Coefficient of performance
DSF	double-skin facade
E	energy (kWh)
EER	energy efficiency ratio (-)
EHP	electric heat pump
h_c	interfacial boundary conductance (W/m^2K)
I_{vert}	vertical pyranometer on the south wall (W/m^2)
k_{3D}	thermal conductivity of the 3D printed materials (W/mK)
k_d	thermal conductivity of the filler (W/mK)
k_m	thermal conductivity of the selected 3D printable polymers (W/mK)
MAE	Mean Absolute Error (°C)
ME	Mean Error (°C)
N	number of measurements (-)
OVF	opaque ventilated facades
PC	proposed case
PES	non-renewable primary energy saving (%)
PET	polyethylene terephthalate
PETG	polyethylene terephthalate glycol-modified
PLA	polylactic acid
RC	reference case
$RMSE$	Root Mean Square Error (°C)
T	thermocouple/temperature (°C)
U	transmittance value (m^2K/W)
V_d	volume fraction of the filler
W	airspeed sensor
Greeks	
Δ	difference
η	efficiency (%)
Subscripts/Superscripts	
cavity	air cavity of the second-skin system
cool	cooling
el	electricity
exp,i	experimental value at time step i
indoor	indoor air
p	non-renewable primary energy
PC	proposed case
PP	power plant
RC	reference case
sim,i	simulated value at time step i
th	thermal
w	window

References

1. European Commission Energy Performance of Buildings Directive. Available online: https://ec.europa.eu/energy/topics/energy-efficiency/energy-efficient-buildings/energy-performance-buildings-directive_en (accessed on 4 August 2020).
2. Antonov, Y.I.; Heiselberg, P.; Flourentzou, F.; Pomianowski, M.Z. Methodology for evaluation and development of refurbishment scenarios for multi-story apartment buildings, applied to two buildings in Denmark and Switzerland. *Buildings* **2020**, *10*, 102. [CrossRef]

3. Cortiços, N.D. Improving residential building efficiency with membranes over facades: The Mediterranean context. *J. Build. Eng.* **2020**, *32*, 101421. [CrossRef]
4. Ascione, F.; Bianco, N.; Maria Mauro, G.; Napolitano, D.F. Building envelope design: Multi-objective optimization to minimize energy consumption, global cost and thermal discomfort. Application to different Italian climatic zones. *Energy* **2019**, *174*, 359–374. [CrossRef]
5. Scorpio, M.; Ciampi, G.; Rosato, A.; Maffei, L.; Masullo, M.; Almeida, M.; Sibilio, S. Electric-driven windows for historical buildings retrofit: Energy and visual sensitivity analysis for different control logics. *J. Build. Eng.* **2020**, *31*, 101398. [CrossRef]
6. Cattarin, G.; Causone, F.; Kindinis, A.; Pagliano, L. Outdoor test cells for building envelope experimental characterization—A literature review. *Renew. Sustain. Energy Rev.* **2016**, *54*, 606–625. [CrossRef]
7. Barbosa, S.; Ip, K. Perspectives of double skin facades for naturally ventilated buildings: A review. *Renew. Sustain. Energy Rev.* **2014**, *40*, 1019–1029. [CrossRef]
8. Ballarini, I.; De Luca, G.; Paragamyan, A.; Pellegrino, A.; Corrado, V. Transformation of an office building into a nearly zero energy building (NZEB): Implications for thermal and visual comfort and energy performance. *Energies* **2019**, *12*, 895. [CrossRef]
9. Sibilio, S.; Rosato, A.; Scorpio, M.; Iuliano, G.; Ciampi, G.; Vanoli, G.P.; de Rossi, F. A Review of Electrochromic Windows for Residential Applications. *Int. J. Heat Technol.* **2016**, *34*, S481–S488. [CrossRef]
10. Ciampi, G.; Rosato, A.; Scorpio, M.; Sibilio, S. Energy and economic evaluation of retrofit actions on an existing historical building in the south of Italy by using a dynamic simulation software. *Energy Procedia* **2015**, *78*, 741–746. [CrossRef]
11. Scorpio, M.; Ciampi, G.; Spanodimitriou, Y.; Rosato, A.; Laffi, R.; Almeida, M.; Sibilio, S. GEMINI: Test Cells for the Acoustic, Visual and Thermal Performances Evaluation of Double-Skin Facades. In Proceedings of the 14th Conference on Sustainable Development of Energy, Water and Environment Systems, Dubrovnik, Croatia, 1–6 October 2019; pp. 1–13.
12. Ciampi, G.; Scorpio, M.; Spanodimitriou, Y.; Rosato, A.; Sibilio, S. Thermal model validation of an electric-driven smart window through experimental data and evaluation of the impact on a case study. *Build. Environ.* **2020**, *181*, 107134. [CrossRef]
13. Krstić-Furundžić, A.; Vujošević, M.; Petrovski, A. Energy and environmental performance of the office building facade scenarios. *Energy* **2019**, *183*, 437–447. [CrossRef]
14. Mejía, K.J.; Barbero-Barrera, M.D.M.; Pérez, M.R. Evaluation of the impact of the envelope system on thermal energy demand in hospital buildings. *Buildings* **2020**, *10*, 250. [CrossRef]
15. Saroglou, T.; Theodosiou, T.; Givoni, B.; Meir, I.A. Studies on the optimum double-skin curtain wall design for high-rise buildings in the Mediterranean climate. *Energy Build.* **2020**, *208*, 109641. [CrossRef]
16. Ghaffarianhoseini, A.; Ghaffarianhoseini, A.; Berardi, U.; Tookey, J.; Li, D.H.W.; Kariminia, S. Exploring the advantages and challenges of double-skin façades (DSFs). *Renew. Sustain. Energy Rev.* **2016**, *60*, 1052–1065. [CrossRef]
17. Chen, X.; Yang, H.; Peng, J. Energy optimization of high-rise commercial buildings integrated with photovoltaic facades in urban context. *Energy* **2019**, *172*, 1–17. [CrossRef]
18. Cerón, I.; Caamaño-Martín, E.; Neila, F.J. "State-of-the-art" of building integrated photovoltaic products. *Renew. Energy* **2013**, *58*, 127–133. [CrossRef]
19. Ibañez-Puy, M.; Vidaurre-Arbizu, M.; Sacristán-Fernández, J.A.; Martín-Gómez, C. Opaque Ventilated Façades: Thermal and energy performance review. *Renew. Sustain. Energy Rev.* **2017**, *79*, 180–191. [CrossRef]
20. Stazi, F.; Ulpiani, G.; Pergolini, M.; Di Perna, C.; D'Orazio, M. The role of wall layers properties on the thermal performance of ventilated facades: Experimental investigation on narrow-cavity design. *Energy Build.* **2020**, *209*, 109622. [CrossRef]
21. Poirazis, H. Division of Energy and Building Design. In *Double Skin Façades for Office Buildings*; Department of Construction and Architecture, Lund University: Lund, Sweden, 2004; ISBN 9185147028.
22. Belleri, A.; Tarantino, S.; Lollini, R.; Arlati, E. Measurement and prediction of heat transfer and mass flow of a ventilated façade. In Proceedings of the AIRAH and IBPSA's Australasian Building Simulation 2017 Conference, Melbourne, Australia, 15–16 November 2017; pp. 1–15.
23. Alberto, A.; Ramos, N.M.M.; Almeida, R.M.S.F. Parametric study of double-skin facades performance in mild climate countries. *J. Build. Eng.* **2017**, *12*, 87–98. [CrossRef]
24. Souza, L.C.O.; Souza, H.A.; Rodrigues, E.F. Experimental and numerical analysis of a naturally ventilated double-skin façade. *Energy Build.* **2018**, *165*, 328–339. [CrossRef]
25. Kuznik, F.; Catalina, T.; Gauzere, L.; Woloszyn, M.; Roux, J. Numerical modelling of combined heat transfers in a double skin façade Full-scale laboratory experiment validation. *Appl. Therm. Eng.* **2011**, *31*, 3043–3054. [CrossRef]
26. Aparicio-Fernández, C.; Vivancos, J.L.; Ferrer-Gisbert, P.; Royo-Pastor, R. Energy performance of a ventilated façade by simulation with experimental validation. *Appl. Therm. Eng.* **2014**, *66*, 563–570. [CrossRef]
27. Diallo, T.M.O.; Zhao, X.; Dugue, A.; Bonnamy, P.; Javier Miguel, F.; Martinez, A.; Theodosiou, T.; Liu, J.S.; Brown, N. Numerical investigation of the energy performance of an Opaque Ventilated Façade system employing a smart modular heat recovery unit and a latent heat thermal energy system. *Appl. Energy* **2017**, *205*, 130–152. [CrossRef]
28. E2VENT Energy Efficient Ventilated Facades for Optimal Adaptability and Heat Exchange. Available online: http://www.e2vent.eu/ (accessed on 12 May 2020).
29. Pergolini, M.; Ulpiani, G.; Shehi, O.; Di Perna, C.; Stazi, F. Controlled inlet airflow in ventilated facades: A numerical analysis. *IOP Conf. Ser. Mater. Sci. Eng.* **2019**, *609*, 032009. [CrossRef]
30. EnergyPlus, Energy Simulation Software. Available online: https://energyplus.net/ (accessed on 29 March 2021).

31. Transient System Simulation Tool TRNSYS 18. Available online: http://www.trnsys.com/demo/ (accessed on 12 May 2020).
32. Trubiano, F. Performance based envelopes: A theory of spatialized skins and the emergence of the integrated design professional. *Buildings* **2013**, *3*, 689–712. [CrossRef]
33. Krivoshapko, S.N. The perspectives of application of thin-walled plastic and composite polymer shells in civil and industrial architecture. *J. Reinf. Plast. Compos.* **2018**, *37*, 217–229. [CrossRef]
34. Agarwal, S.; Gupta, R.K. *Plastics in Buildings and Construction*, 2nd ed.; Elsevier Inc.: Amsterdam, The Netherlands, 2017; ISBN 9780323390408.
35. Moradibistouni, M.; Vale, B.; Isaacs, N. Evaluating the use of polymers in residential buildings: Case study of a single storey detached house in New Zealand. *J. Build. Eng.* **2020**, *32*, 101517. [CrossRef]
36. Project DWG the Pet Pavilion, Public Space in a Changing Society. Available online: https://www.projectdwg.com/the-pet-pavilion-public-space-in-a-changing-society-in-enschede-by-projectdwg/ (accessed on 2 February 2021).
37. Loos.Fm the Pet Pavilion, Public Space in a Changing Society. Available online: http://loos.fm/en/project-pet-pavilion.php (accessed on 2 February 2021).
38. The Far Eastern Group EcoARK-World's First PET Bottle Green Building. Available online: https://www.expopark.taipei/en/cp.aspx?n=175 (accessed on 2 February 2021).
39. Moretti, E.; Zinzi, M.; Belloni, E. Polycarbonate panels for buildings: Experimental investigation of thermal and optical performance. *Energy Build.* **2014**, *70*, 23–35. [CrossRef]
40. Čekon, M.; Šikula, O. Experimental and numerical study on the thermal performance of polycarbonate panels. *J. Build. Eng.* **2020**, *32*, 101715. [CrossRef]
41. Construcciones Planificadas Hotel Grand Hyatt Bogotá. Available online: http://www.construccionesplanificadas.com/en/ (accessed on 2 February 2021).
42. Hager, I.; Golonka, A.; Putanowicz, R. 3D Printing of Buildings and Building Components as the Future of Sustainable Construction? *Procedia Eng.* **2016**, *151*, 292–299. [CrossRef]
43. Sakin, M.; Kiroglu, Y.C. 3D Printing of Buildings: Construction of the Sustainable Houses of the Future by BIM. *Energy Procedia* **2017**, *134*, 702–711. [CrossRef]
44. 3Dprint 3D Printed Building Facades. Available online: https://3dprint.com/187220/3d-printed-building-facades/%0A (accessed on 2 February 2021).
45. ARCHELLO 3D Printed Facade for Eu-Building. Available online: https://archello.com/en/project/3d-printed-facade-for-eu-building (accessed on 2 February 2021).
46. Sarakinioti, M.V.; Turrin, M.; Konstantinou, T.; Tenpierik, M.; Knaack, U. Developing an integrated 3D-printed façade with complex geometries for active temperature control. *Mater. Today Commun.* **2018**, *15*, 275–279. [CrossRef]
47. Vidakis, N.; Petousis, M.; Tzounis, L.; Maniadi, A.; Velidakis, E.; Mountakis, N.; Papageorgiou, D.; Liebscher, M.; Mechtcherine, V. Sustainable additive manufacturing: Mechanical response of polypropylene over multiple recycling processes. *Sustainability* **2021**, *13*, 159. [CrossRef]
48. Shemelya, C.; De La Rosa, A.; Torrado, A.R.; Yu, K.; Domanowski, J.; Bonacuse, P.J.; Martin, R.E.; Juhasz, M.; Hurwitz, F.; Wicker, R.B.; et al. Anisotropy of thermal conductivity in 3D printed polymer matrix composites for space based cube satellites. *Addit. Manuf.* **2017**, *16*, 186–196. [CrossRef]
49. Labonnote, N.; Rønnquist, A.; Manum, B.; Rüther, P. Additive construction: State-of-the-art, challenges and opportunities. *Autom. Constr.* **2016**, *72*, 347–366. [CrossRef]
50. Yazdani Sarvestani, H.; Akbarzadeh, A.H.; Niknam, H.; Hermenean, K. 3D printed architected polymeric sandwich panels: Energy absorption and structural performance. *Compos. Struct.* **2018**, *200*, 886–909. [CrossRef]
51. Hasselman, D.P.H.; Johnson, L.F. Effective Thermal Conductivity of Composites with Interfacial Thermal Barrier Resistance. *J. Compos. Mater.* **1987**, *21*, 508–515. [CrossRef]
52. University of Campania Luigi Vanvitelli; Department of Architecture and Industrial Design Ri.A.S.-Built Environment Control Laboratory. Available online: https://www.architettura.unicampania.it/images/ricerca/laboratori/EN/0-Lab_RIAS_ENG_30042020.pdf (accessed on 4 September 2020).
53. Batlles, F.J.; Olmo, F.J.; Alados-Arboledas, L. On shadowband correction methods for diffuse irradiance measurements. *Sol. Energy* **1995**, *54*, 105–114. [CrossRef]
54. Ensinger TECARAN ABS Grey. Available online: https://www.ensingerplastics.com/en/shapes/products/tecaran-abs-grey (accessed on 10 February 2021).
55. Dickinson, E.W. *Solar Energy Technology Handbook*; CRC Press: Boca Raton, FL, USA, 2017; ISBN 9781351076739.
56. Al-Saadi, S.N.; Zhai, Z. A new validated TRNSYS module for simulating latent heat storage walls. *Energy Build.* **2015**, *109*, 274–290. [CrossRef]
57. Vahidi Bidhendi, M.; Abbassi, Y. Exploring dynamic operation of a solar dish-stirling engine: Validation and implementation of a novel TRNSYS type. *Sustain. Energy Technol. Assess.* **2020**, *40*, 100765. [CrossRef]
58. Yasin, M.; Scheidemantel, E.; Klinker, F.; Weinläder, H.; Weismann, S. Generation of a simulation model for chilled PCM ceilings in TRNSYS and validation with real scale building data. *J. Build. Eng.* **2019**, *22*, 372–382. [CrossRef]
59. TRNSYS 18 TRNSYS Manual-Volume 3, Standard Component Library Overview. Available online: http://www.trnsys.com/assets/docs/03-ComponentLibraryOverview.pdf (accessed on 4 September 2020).

60. Solar Energy Laboratory, University of Wisconsin-Madison and Thermal Energy System Specialists. *Thermal Energy Systems Specialists TRNSYS Manual-Volume 4, Mathematical Reference*; Solar Energy Laboratory, University of Wisconsin-Madison: Madison, WI, USA, 2018; pp. 1–705.
61. TESS Component Library TESS Individual Components-TYPE 1230: Ventilated Air Cavity Wall (Ventilated Facade). Available online: http://www.trnsys.com/tess-libraries/individual-components.php.html (accessed on 14 March 2021).
62. Trimble Inc. SketchUp Pro 2014. Available online: https://3dwarehouse.sketchup.com/model/ua1d8251e-be08-4735-89c3-008b8e79ff3d/sketchUp-pro-2014?hl=it (accessed on 4 September 2020).
63. Italian Government DM 26 Giugno 2015. Available online: https://www.mise.gov.it/index.php/it/normativa/decreti-interministeriali/2032966-decreto-interministeriale-26-giugno-2015-applicazione-delle-metodologie-di-calcolo-delle-prestazioni-energetiche-e-definizione-delle-prescrizioni-e-dei-requisiti-minimi-degli-edifici (accessed on 4 September 2020).
64. G.I. Industrial Holding Technical Brochure-CRA/K 15÷131. Available online: https://clint.it/en/products/aircooled-liquid-chillers-and-heat-pumps-for-commercial-industrial-application-2/aircooled-liquid-chillers-and-heat-pumps/crak-15131/ (accessed on 4 September 2020).
65. García, E.; De Pablos, A.; Bengoechea, M.A.; Guaita, L.; Osendi, M.I.; Miranzo, P. Thermal conductivity studies on ceramic floor tiles. *Ceram. Int.* **2011**, *37*, 369–375. [CrossRef]
66. MakeItFrom.com. Glycol-Modified Polyethylene Terephthalate (PETG). Available online: https://www.makeitfrom.com/material-properties/Glycol-Modified-Polyethylene-Terephthalate-PETG-PET-G (accessed on 2 February 2020).
67. MakeItFrom.com. Polylactic Acid (PLA, Polylactide). Available online: https://www.makeitfrom.com/material-properties/Polylactic-Acid-PLA-Polylactide (accessed on 2 February 2020).
68. SD3D ABS Technical Data Sheet. Available online: https://www.sd3d.com/wp-content/uploads/2015/10/MaterialTDS-ABS-Web.pdf (accessed on 10 February 2021).
69. SD3D PETG Technical Data Sheet. Available online: https://www.sd3d.com/wp-content/uploads/2017/06/MaterialTDS-PETG_01.pdf (accessed on 10 February 2021).
70. SD3D PLA Technical Data Sheet. Available online: https://www.sd3d.com/wp-content/uploads/2017/06/MaterialTDS-PLA_01.pdf (accessed on 10 February 2021).
71. Stephan, K.; Laesecke, A. The Thermal Conductivity of Fluid Air. *J. Phys. Chem. Ref. Data* **1985**, *14*, 227–234. [CrossRef]
72. Ente Nazionale Italiano di Unificazione. *Energy Performance of Buildings Part 1: Evaluation of Energy Need for Space Heating and Cooling*; UNI/TS 11300-1; Ente Nazionale Italiano di Unificazione (UNI): Room, Italy, 2014.
73. Euporpean Committee for Standardzation. *Heating Systems in Buildings–Method for Calculation of the Design Heat Load*; EN 12831:2003 E; Euporpean Committee for Standardzation: Brussels, Belgium, 2003.
74. Rosato, A.; Ciervo, A.; Ciampi, G.; Scorpio, M.; Guarino, F.; Sibilio, S. Impact of solar field design and back-up technology on dynamic performance of a solar hybrid heating network integrated with a seasonal borehole thermal energy storage serving a small-scale residential district including plug-in electric vehicles. *Renew. Energy* **2020**, *154*, 684–703. [CrossRef]
75. Angrisani, G.; Canelli, M.; Roselli, C.; Russo, A.; Sasso, M.; Tariello, F. A small scale polygeneration system based on compression/absorption heat pump. *Appl. Therm. Eng.* **2017**, *114*, 1393–1402. [CrossRef]
76. SIA 2024:2015-Dati D'utilizzo di Locali per L'energia e L'impiantistica Degli Edifici. Available online: https://www.sia.ch/en/the-sia/ (accessed on 4 September 2020).
77. Veglas. Veglas s.r.l. Available online: http://www.veglas.it (accessed on 20 March 2021).
78. Plasting. Plasting s.r.l. Available online: https://www.plasting.biz/en/ (accessed on 20 March 2021).
79. SD3D. SD3D Printing. Available online: https://www.sd3d.com (accessed on 20 March 2021).